

# Structural Contributions to Charge Transport across Ni-Octanedithiol Multilayer Junctions

Lam H. Yu, Christopher D. Zangmeister, and James G. Kushmerick\*

National Institute of Standards and Technology, Gaithersburg, Maryland 20899

Received August 9, 2006; Revised Manuscript Received September 14, 2006

## ABSTRACT

We report the fabrication and characterization of multilayer thin films incorporating 1,8-octanedithiols and Ni atoms. Low-temperature charge transport measurements exhibit inelastic co-tunneling and resonant tunneling features that correspond energetically to vibrational excitations of the molecular multilayer. Several junctions exhibit changes in conductance features characteristic of charge defect-gating. Transport through our junctions is shown to be dominated by the intrinsic properties of the multilayer.

One of the primary challenges of molecular electronics is to definitively identify the origin of the transport characteristics observed in a given device. Various experiments have demonstrated that the electrode-molecule contact can be as important as the intrinsic chemical nature of the molecules in determining the charge transport through a molecular device.<sup>1–5</sup> In some cases, it has even been shown that the transport characteristics are completely independent of the molecule and are solely a result of the electrodes and device fabrication.<sup>6</sup> Measuring vibronic coupling between the charge carrier and the molecular system has become an important tool for identifying the molecular component of the observed transport characteristics.<sup>7–10</sup>

In this letter, we demonstrate how the transport characteristics of a molecular junction can be directly influenced by the active design of the molecular component. Using 1,8-octanedithiol and Ni(II) ions as the building blocks of our molecular device, we employed a bottom-up approach to assemble multilayer structures which exhibit transport behavior commensurate with the structural design of the molecular multilayer. A previous study of ruthenium-based multilayer films in thick-film ( $\approx 30$  molecular layers), planar-geometry devices has yielded single-cycle switching behavior attributed to irreversible oxidation of the ruthenium atoms.<sup>11</sup> The multilayer molecular junctions reported here, which consist of only three octanedithiol layers, exhibit stochastic gating due to time varying charging of defects in the molecular multilayer. We also observe vibrational excitations via both nonresonant and resonant electron tunneling which match the known and calculated vibrational spectra of the molecular multilayer.

The method for multilayer formation reported in this letter is based on previous work done on Cu-dithiol multilayer thin films.<sup>12</sup> For ellipsometry, external reflectance Fourier transform infrared spectroscopy (FTIR), and X-ray photoelectron spectroscopy (XPS) measurements, the Ni-octanedithiol multilayer thin films (NOMTFs) were prepared on thermally evaporated gold substrates. The NOMTFs were constructed by first immersing a gold substrate into a 3 mM solution of 1,8-octanedithiol (**C8**) in 2-propanol for approximately 14 h. The substrate was then sonicated in fresh 2-propanol for 5 min and dried with a jet of nitrogen. After confirmation of monolayer formation by ellipsometry and FTIR, the substrate was exposed to a 35 mM Ni(ClO<sub>4</sub>)<sub>2</sub>·6H<sub>2</sub>O solution in 2-propanol for 3 h. Following the thiol reaction with the Ni (II) containing solution, the substrate was cleaned and dried as before. Additional layers are formed by repetitions of these procedures. The NOMTF on thin Au wire (diameter 10  $\mu$ m) used in the crossed-wire tunnel junction experiments were constructed by the same method. No multilayer formation was observed if the samples were not exposed to the Ni(II) solution.

Figure 1a plots the ellipsometric thickness as a function of the number of **C8** depositions. The slope of the best-fit line through the ellipsometric data gives an average monolayer thickness of 1.3 nm. Note that since each ellipsometric measurement is taken after the **C8** deposition, the measured differential change in layer thickness is different between the first layer and all subsequent layers. The ellipsometric measurement of the first layer reflects the thickness of a single **C8** monolayer (theoretical thickness = 1.15 nm), but the ellipsometric measurement of each subsequent layer reflects the addition of half a monolayer of Ni ions (see XPS data discussion below) in addition to a **C8** monolayer

\* To whom correspondence should be addressed. E-mail: james.kushmerick@nist.gov.

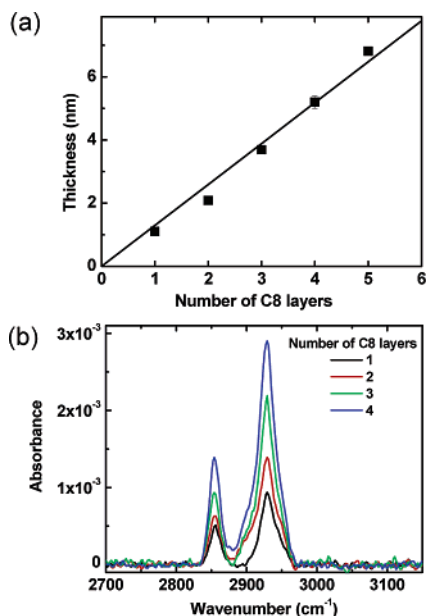


**Figure 1.** (a) Ellipsometric thickness of **C8**-Ni multilayer thin films on gold as a function of the number of **C8** layers deposited. (b) Comparison of FTIR spectra of a **C8** monolayer and **C8**-Ni multilayers.

(theoretical thickness = 1.32 nm). The linear increase in thickness demonstrates the formation of an ordered multilayer system.<sup>12,13</sup> For the ellipsometric thickness reported, we have assumed a value of 1.45 for the refractive index of the multilayer in accordance with previous ellipsometric studies of alkanedithiol-based multilayers.<sup>12</sup>

Figure 1b shows the evolution of the FTIR spectrum of the NOMTFs as successive layers of **C8** and Ni are deposited. The two aliphatic  $\text{CH}_2$  stretching modes,  $\nu_{\text{as}}(\text{C}-\text{H})$  and  $\nu_{\text{s}}(\text{C}-\text{H})$  at 2929 and 2854  $\text{cm}^{-1}$ , respectively, are shown to increase in strength as the thickness of the multilayer increases. The absorbance integrals of the  $\nu_{\text{as}}(\text{C}-\text{H})$  and  $\nu_{\text{s}}(\text{C}-\text{H})$  bands are linearly related to the number of **C8** layers in the multilayer (see the Supporting Information). No appreciable shift in frequency in the FTIR spectrum is observed as the number of layer increases, which indicates no change in layer disorder as new layers are added.

NOMTFs prepared on Au were examined by XPS to further explore the structure of the multilayer films as well as determine the Ni oxidation state. The XPS spectrum of a single layer of Ni adsorbed to a monolayer of **C8** reveals that we get  $\approx 50\%$  coverage of Ni atoms. This trend of 50% Ni coverage continues to hold as successive layers of **C8** and Ni are added. The Ni coverage is determined from the ratio of Ni to unbounded S at each layer. No appreciable Cl concentration was detected by XPS confirming that the measured Ni signal is from bound Ni and not from residue of the Ni-perchlorate salt. A table detailing the atomic concentration of various relevant elements in the multilayers is given in the Supporting Information. It is important to note that, although we only have 50% coverage of Ni in any layer, the presence of Ni is required for multilayer formation, likely through catalyzation of interlayer disulfide linkages.<sup>13</sup>

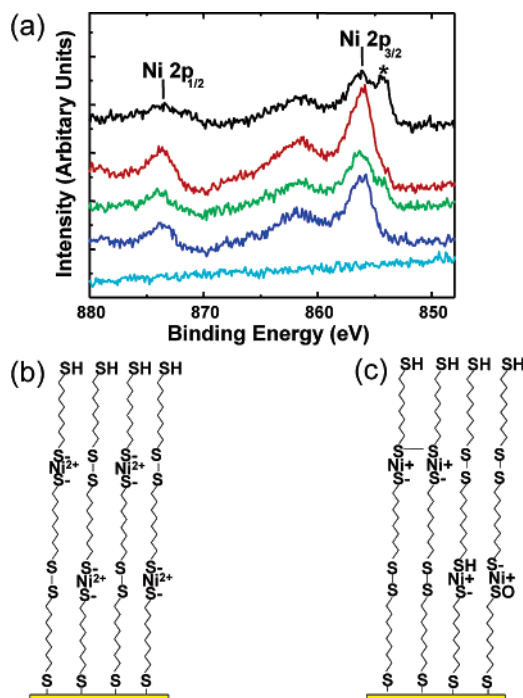


**Figure 2.** (a) XPS spectra of the Ni 2p region of monolayer **C8** and multilayers of various thicknesses. The spectra from the bottom to top are of Au/**C8**, Au/**C8**-Ni, Au/**C8**-Ni-**C8**, Au/**C8**-Ni-**C8**-Ni, and Au/**C8**-Ni-**C8**-Ni-**C8** (spectra are offset for clarity). The peaks at 856 and 873.7 eV are characteristic of Ni(II). The feature at 854.5 eV marked by an asterisk indicates between 10% and 30% of the Ni in the multilayer are Ni(I). (b) Proposed model of the multilayer structure with Ni(II). (c) Proposed model of the multilayer structure with Ni(I).

Figure 2a shows the Ni 2p region for different steps in the multilayer assembly process (a similar plot for the S 2p region is given in the Supporting Information). The bottom spectrum is for a single **C8** monolayer, and each successive spectrum adds a layer of Ni or **C8**, with the top spectrum from a multilayer thin film composed of three **C8** and two Ni layers. All of the spectra in Figure 2a, except the monolayer spectrum show three distinctive Ni features. The positions of the two peaks which represent the binding energies of the Ni  $2p_{3/2}$  electrons and Ni  $2p_{1/2}$  electrons, at 856 and 873.7 eV, respectively, as well as the presence of the satellite feature at 861 eV, gives clear evidence that the majority of the Ni atoms in the multilayer film are in the +2 oxidation state.<sup>14</sup>

We attribute the feature at 854.5 eV indicated by an asterisk in Figure 2a, to the presence of Ni(I) in our multilayer structures. The fact that the Ni(I) peak is not present in the initial Au/**C8**-Ni structure (dark blue trace Figure 2a) suggests that some Ni is reduced from the +2 to +1 oxidation state upon deposition of a second **C8** layer. The presence of the broad satellite feature centered at 861 eV makes a precise analysis of the Ni(I)/Ni(II) ratio difficult; however, we estimate that between 70% and 90% of the Ni atoms in the multilayer structure are Ni(II). The Ni(I) feature from the buried Ni layer in the Au/**C8**-Ni-**C8**-Ni XPS spectrum (red trace Figure 2a) is most likely obscured by the strong intensity of Ni(II) at the multilayer surface.

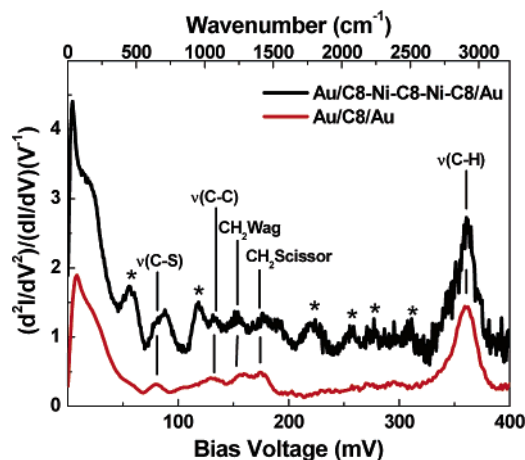


**Figure 3.** IET spectra of a C8-Ni-C8-Ni-C8 multilayer junction (black) and a C8 monolayer junction (red). The black trace is shifted vertically by  $0.5 \text{ V}^{-1}$  for clarity. The peak feature at low energy is the result of ZBF as discussed in the text. Mode assignments are from comparison to previous experimental results and DFT calculations (see text). The asterisks mark the IETS modes observed only in the multilayer junction.

Due to the presence of Ni(I) in our multilayers, we cannot rule out the possibility of intralayer disulfide bonding in the C8 layer as has been previously observed for Cu-dithiol multilayers.<sup>12,13</sup> Figure 2, panels b and c, shows two possible multilayer film structures with the structure in Figure 2b representing 70–90% of our film. We note that, to accommodate the presence of Ni(I) in our NOMTF, intralayer disulfide bonding is only one possible scenario. The sulfurs in the NOMTF could also retain their hydrogen or become oxidized. In fact, there are indications from the transport measurements of the NOMTF-based tunnel junctions that S–H and S–O bonds exist in the multilayer film.

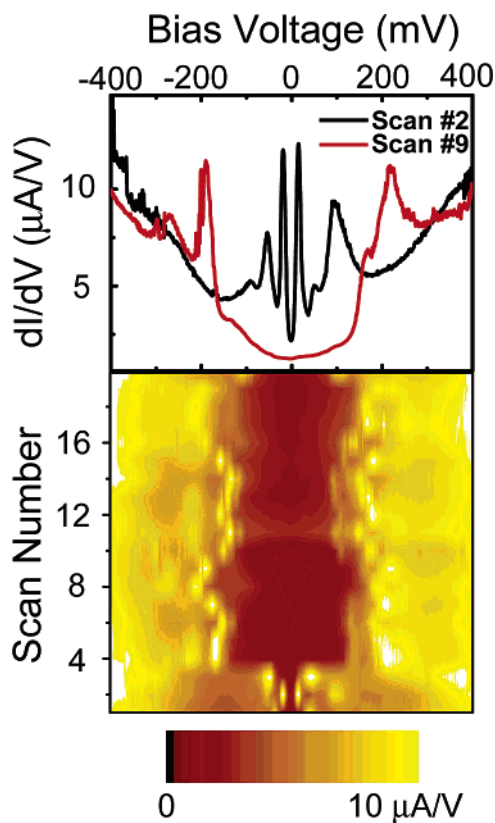
Transport measurements of NOMTFs were performed with a custom-built cryogenic crossed-wire tunneling junction apparatus as reported previously.<sup>7</sup> Briefly, two 10  $\mu\text{m}$  diameter Au wires, one coated with the NOMTF, are mounted inside a stainless steel vacuum can that is evacuated and purged with He gas before being lowered into a liquid He storage dewar. The crossed-wire tunnel junction is allowed to equilibrate for at least 1 h before transport measurements are made. All transport measurements were made at liquid He temperature. Transport measurements are performed with a computer controlled DAQ card and external current preamplifier. Standard ac modulation techniques along with two lock-in amplifiers are used to record the first and second harmonic signals (proportional to  $dI/dV$  and  $d^2I/dV^2$ , respectively) simultaneously with the current–voltage ( $I$ – $V$ ) characteristics. A modulation amplitude of 4 mV was used for all transport measurements of NOMTF-based junctions. We refer to the normalized second derivative signal  $(d^2I/dV^2)/(dI/dV)$  as the inelastic electron tunneling (IET) spectrum.<sup>15</sup>

Figure 3 shows the IET spectra of a NOMTF junction containing three layers of C8 and two layers of Ni (in black) as well as a junction formed from a single C8 monolayer (in red). Features which are common to both the multilayer and monolayer junctions are labeled with their assigned

vibrational modes, whereas the features which appear exclusively in the multilayer junction are labeled with an asterisk. The features which appear both in the C8 monolayer junction and the NOMTF junction can be assigned to specific molecular vibrations based on previous spectroscopic studies of alkenethiolate monolayers.<sup>7,8,16–18</sup> The most intense vibrational mode observed is the C–H stretch at 362 mV. We also observe four less intense peaks at 175, 159, 132, and 80 mV, corresponding to CH<sub>2</sub> scissoring, CH<sub>2</sub> wagging, C–C stretching, and C–S stretching, respectively. The zero-bias feature (ZBF) which extends out to  $\sim 30$  mV from zero bias is believed to originate from phonon interactions in the gold wires and is unrelated to the molecules in the junctions.<sup>19,20</sup> It is important to note that our C8 IET spectrum is significantly different than that previously reported by Reed and co-workers<sup>8</sup> but is consistent with our earlier undecanethiol spectrum.<sup>7</sup> Clearly in light of the prominent C–H stretching mode observed for the C8 monolayer, the observation of the C–H stretching mode in our previous study cannot be solely attributed to the terminal methyl group as suggested by some calculations.<sup>21–24</sup>

Although Figure 3 clearly shows that all of the vibrational features observed in the monolayer sample are also present in the multilayer junction, there are two regions, one below 125 mV (region I) and another between 185 mV and 310 mV (region II), where additional features are observed. To aid in assignment of these vibrational modes, density functional theory (DFT) calculations were performed for C8 molecules bound to Au and Ni atoms as well as for two alkyl thiols bridged by a single Ni atom. Most interesting among these new vibrational features is the mode at 57 mV, which is consistent with the calculated energy for a Ni atom vibrating between two alkyl thiolates. This mode thus serves as a vibronic signature for our multilayer structure. The DFT calculations suggest that the prominent feature at 118 mV is a C–C backbone mode in which the carbon atoms primarily move parallel to the electrode surface. Although previous IET experiments and theoretical calculations have shown that longitudinal vibrational modes are more dominant in metal–molecule–metal IET spectra,<sup>7,21</sup> the increased conformational freedom afforded by the multilayer structures may account for the strong intensity of this transverse mode. The origin of the IETS features in region II is less clear. We can assign the weak IETS feature at the high-energy end of region II, at 310 mV, to the S–H stretching mode. From our XPS experiments, we know that a small fraction of the sulfur in the multilayer thin film is oxidized ( $\approx 6\%$ ), suggesting that the other features may be associated with S–O vibrational modes. Although S–O modes are normally confined to the low-energy end of region II, these vibrational modes could be shifted to higher energy by the physical compression applied to the layers during the measurements or by excess charges on the oxidized sulfurs. Some transport data, discussed below, indicate that the oxidized sulfurs are indeed sometimes charged. The FTIR spectrum of a C8-Ni-C8-Ni-C8 NOMTF also reveals broad spectral features between 1700 and 2200  $\text{cm}^{-1}$  reminiscent of the unassigned features in regions II (see the Supporting Information).





**Figure 4.** (Top) Differential conductance as a function of bias voltage of a C8-Ni-C8-Ni-C8 multilayer junction in the defect-gating regime. The conductance gap changed by a factor of 10 between the two scans. (Bottom) Color map of the differential conductance  $dI/dV$  as a function of bias voltage and scan number of the same multilayer junction.

Although the FTIR spectrum does not allow us to unambiguously assign specific vibration modes to the features in region II, it does confirm that they originate from intrinsic vibrations of the multilayer structure.

Although the majority of NOMTF devices studied exhibited nonresonant tunneling transport, in a number of our junctions, we observed stochastic gating behavior reminiscent of those observed in gateable Coulomb blockade molecular devices.<sup>9,25–28</sup> Figure 4 shows an example of a C8-Ni-C8-Ni-C8 NOMTF tunnel junction which exhibits such stochastic gating behavior. The bottom of Figure 4 is a conductance map of the device where the  $x$  axis is the bias voltage applied across the cross-wire junction; the  $y$  axis is the scan number, and the contrast represents the device conductance. The top of Figure 4 shows two slices of the conductance map.

In general, Coulomb blockade occurs when a confined electronic system (called an island) is weakly coupled to source and drain electrodes. At low bias, nonresonant tunneling is the dominant transport mechanism. When the bias voltage applied is sufficient to align an energy level of the island with the Fermi level of an electrode, resonant transport commences and the Coulomb blockade is lifted. The bias voltage required to initiate resonant transport thus defines the conductance gap of the device. In three terminal devices, a capacitively coupled gate electrode can control

the conductance gap by tuning the offset between island energy levels and the electrode Fermi level. In our devices, the NOMTF incorporated with an array of Ni atoms, tunnel coupled to two gold electrodes, acts as a confined electronic system.

Although our cross-wire tunnel junctions are two-terminal devices that do not incorporate a gate electrode, the conductance gap in Figure 4 fluctuates between 17 and 200 mV. Uncontrolled gating is occasionally observed in single-molecule transistor devices due to traps present in the gate oxide.<sup>29</sup> The sulfones (S–O) present in our NOMTFs (as indicated by the XPS and IET measurements) likely act as local charge defects resulting in the stochastic gating observed in Figure 4.

Whereas IET spectra arise from nonresonant inelastic co-tunneling via virtual excitation of molecular vibrational states,<sup>30</sup> vibronic contributions to charge transport via resonant tunneling have been previously observed in devices exhibiting Coulomb blockade behavior as satellite peaks outside the conductance gap.<sup>25,27,29,31,32</sup> Such vibronic satellite peaks are visible in the conductance plots for our NOMTF device shown in Figure 4. In Figure 4 (top), we plotted the scan of the device when it has the smallest conductance gap ( $\approx 17$  mV) and a more representative scan of the device when it has a conductance gap  $\approx 200$  mV. In both scans, we observe secondary peak features above the edge of the conductance gap. In fact, every scan of the device as shown in Figure 4 (bottom) exhibits at least one secondary peak feature in its conductance. Although the electronic couplings of the NOMTF device shown in Figure 4 are relatively symmetric as evidenced by the symmetric shape of its conductance gaps, the amplitude of the satellite peaks does show noticeable bias polarity asymmetry. This asymmetry is directly attributable to the vibronic origin of these satellite peaks. As will be discussed below, the satellite peaks originate from a S–Ni–S bending mode in the multilayer, and as a result of the geometry of the NOMTF, any Ni-based vibration will exhibit some degree of bias polarity asymmetry due to its asymmetric placement with respect to the two electrodes.<sup>33</sup>

Electronic excitation through multiple-barrier tunnel junctions has been shown to exhibit multiple conductance peaks with variable spacing and amplitude.<sup>34</sup> However, the fact that the value of the conductance gaps of our device varies from 17 to 200 mV while the energy spacings between their first and second peaks increases with the size of the conductance gap, but remain comparatively small ( $< 80$  mV), makes such interpretation unlikely. Based on an analysis of the peak-to-peak distances of the conductance features in the various scans shown in Figure 4, we estimated the energy of a vibrational mode which would give rise to the secondary conductance peaks observed in Figure 4 to be equal to  $36 \pm 5$  mV. DFT calculations predict that a S–Ni–S bending mode exists at 36 mV. As mentioned above, nonresonant tunneling is the dominant transport mechanism inside the Coulomb blockade conductance gap, and thus it follows that it should be possible to observe IET in this region. Figure 5 is the IET spectrum obtained from averaging the low bias

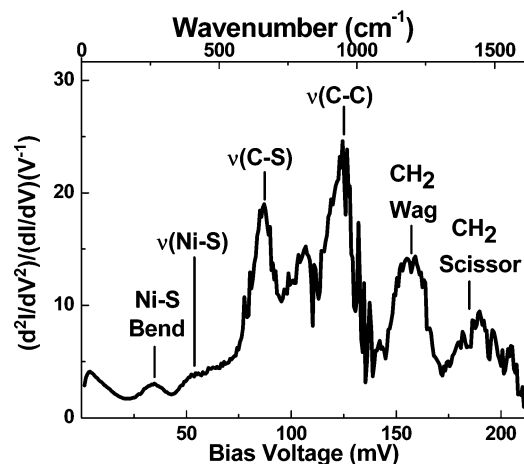


**Figure 5.** IET spectrum of the C8-Ni-C8-Ni-C8 multilayer junction exhibiting stochastic gating behavior shown in Figure 4. This spectrum is the average of scans 4–20 in Figure 4. Note the presence of the Ni–S bending mode at 36 mV, in agreement with our analysis of the satellite peaks in Figure 4.

region ( $|V| < 200$  mV) of scans 4–20 from Figure 4. The IET spectrum confirms the presence of a vibrational mode at 36 mV as well as all of the other prominent features observed below 200 mV in Figure 3. Interestingly, the vibronic coupling is much stronger in the blocked measurements as evidenced by more than a factor of 20 increase in the IET spectrum intensity.

In summary, we have fabricated and characterized multilayer thin film molecular electronic devices based on sequential self-assembly of 1,8-octanedithiol and Ni(II) ions. Incorporation of Ni atoms into the conduction pathway for these devices is confirmed by inelastic electron tunneling spectroscopy. A number of junctions exhibit Coulomb blockade behavior with stochastic charge-defect gating. Resonant tunneling satellite peaks coupled to a S–Ni–S bending mode further highlight the importance of Ni to the charge transport properties of these junctions. We are currently investigating the magnetic and magnetoresistive properties of these multilayer structures.

**Acknowledgment.** The authors thank D. Natelson and J. M. Beebe for useful discussions. The financial support of the Defense Advanced Research Project Agency is gratefully acknowledged.

**Supporting Information Available:** Elemental concentrations and S 2p XPS for multilayer formation, normalized integrated area of the C–H vibrational modes as a function of multilayer deposition, and FTIR spectra for a C8 monolayer and C8-Ni-C8-Ni-C8 multilayer in the 1700–2200  $\text{cm}^{-1}$  region. This material is available free of charge via the Internet at <http://pubs.acs.org>.

## References

- (1) Kushmerick, J. G.; Holt, D. B.; Yang, J. C.; Naciri, J.; Moore, M. H.; Shashidhar, R. *Phys. Rev. Lett.* **2002**, *89* (8), 086802.
- (2) Beebe, J. M.; Engelkes, V. B.; Miller, L. L.; Frisbie, C. D. *J. Am. Chem. Soc.* **2002**, *124*, 11268–11269.
- (3) Salomon, A.; Cahen, D.; Lindsay, S. M.; Tomfohr, J.; Engelkes, V. B.; Frisbie, C. D. *Adv. Mater.* **2003**, *15*, 1881–1890.
- (4) Richter, C. A.; Stewart, D. R.; Ohlberg, D. A. A.; Williams, R. S. *Appl. Phys. A* **2005**, *80*, 1355–1362.
- (5) Kim, B.-S.; Beebe, J. M.; Jun, Y.; Zhu, X. Y.; Frisbie, C. D. *J. Am. Chem. Soc.* **2006**, *128*, 4970–4971.
- (6) Stewart, D. R.; Ohlberg, D. A. A.; Beck, P. A.; Chen, Y.; Williams, R. S.; Jeppesen, J. O.; Nielsen, K. A.; Stoddart, J. F. *Nano Lett.* **2004**, *4*, 133–136.
- (7) Kushmerick, J. G.; Lazorcik, J.; Patterson, C. H.; Shashidhar, R.; Seferos, D. S.; Bazan, G. C. *Nano Lett.* **2004**, *4*, 639–642.
- (8) Wang, W.; Lee, T.; Kretzschmar, I.; Reed, M. A. *Nano Lett.* **2004**, *4*, 643–646.
- (9) Yu, L. H.; Keane, Z. K.; Ciszek, J. W.; Cheng, L.; Stewart, M. P.; Tour, J. M.; Natelson, D. *Phys. Rev. Lett.* **2004**, *93*, 266802.
- (10) Troisi, A.; Ratner, M. A. *Small* **2006**, *2* (2), 172–181.
- (11) Lin, C.; Kagan, C. R. *J. Am. Chem. Soc.* **2003**, *125*, 336–337.
- (12) Brust, M.; Blass, P. M.; Bard, A. J. *Langmuir* **1997**, *13*, 5602–5607.
- (13) Brower, T. L.; Cook, M.; Ulman, A. *J. Phys. Chem. B* **2003**, *107*, 11721–11725.
- (14) Moulder, J. F.; Stickle, W. F.; Sobol, P. E.; Bomben, K. D. *Handbook of X-Ray Photoelectron Spectroscopy*; Perkin-Elmer Corporation: Eden Prairie, MN, 1992.
- (15) Jaklevic, R.; Lambe, J. *Phys. Rev. Lett.* **1966**, *17*, 1139–1140.
- (16) Porter, M. D.; Bright, T. B.; Allara, D. L.; Chidsey, C. E. D. *J. Am. Chem. Soc.* **1987**, *109*, 3559–3568.
- (17) Bryant, M. A.; Pemberton, J. E. *J. Am. Chem. Soc.* **1991**, *113*, 8284–8293.
- (18) Duwez, A.-S.; Yu, L.-M.; Riga, J.; Delhalle, J.; Pireaux, J.-J. *Langmuir* **2000**, *16*, 6569–6576.
- (19) Agnolet, G.; Savitski, S. R.; Zimmerman, D. T. *Physica B* **2000**, *284–288*, 1840–1841.
- (20) Jansen, A.; van Gelder, A.; Wyder, P. *J. Phys. C: Solid State Phys.* **1980**, *13*, 6073–6118.
- (21) Troisi, A.; Ratner, M. A. *Phys. Rev. B* **2005**, *72*, 033408.
- (22) Chen, Y. C.; Zwolak, M.; Di Ventra, M. *Nano Lett.* **2005**, *5*, 621–624.
- (23) Jiang, J.; Kula, M.; Luo, Y. *Nano Lett.* **2005**, *5* (8), 1551–1555.
- (24) Paulsson, M.; Frederiksen, T.; Brandbyge, M. *Nano Lett.* **2006**, *6* (2), 258–262.
- (25) Park, H.; Park, J.; Lim, A. K. L.; Anderson, E. H.; Alivisatos, A. P.; McEuen, P. L. *Nature* **2000**, *407*, 57–60.
- (26) Park, J.; Pasupathy, A. N.; Goldsmith, J. I.; Chang, C.; Yaish, Y.; Petta, J. R.; Rinkoski, M.; Sethna, J. P.; Abruna, H. D.; McEuen, P. L.; Ralph, D. I. *Nature* **2002**, *417*, 722–725.
- (27) Liang, W.; Shores, M. P.; Bockrath, M.; Long, J. R.; Park, H. *Nature* **2002**, *417*, 725–729.
- (28) Getty, S. A.; Engtrakul, C.; Wang, L.; Liu, R.; Ke, S.-H.; Baranger, H. U.; Yang, W.; Fuhrer, M. S.; Sita, L. R. *Phys. Rev. B* **2005**, *71*, 241401.
- (29) Yu, L. H.; Natelson, D. *Nano Lett.* **2004**, *4* (1), 79–83.
- (30) Troisi, A.; Ratner, M. A.; Nitzan, A. *J. Chem. Phys.* **2003**, *118* (13), 6072–6082.
- (31) Qiu, X. H.; Nazin, G. V.; Ho, W. *Phys. Rev. Lett.* **2004**, *92*, 206102.
- (32) Chae, D.; Berry, J. F.; Jung, S.; Cotton, F. A.; Murillo, C. A.; Yao, Z. *Nano Lett.* **2006**, *6* (2), 165–168.
- (33) Galperin, M.; Nitzan, A.; Ratner, M. A.; Stewart, D. R. *J. Phys. Chem. B* **2005**, *109*, 8519–8522.
- (34) Bar-Saden, E.; Goldstein, Y.; Zhang, C.; Deng, H.; Abeles, B.; Millo, O. *Phys. Rev. B* **1994**, *50*, 8961–8964.

NL061867J